Simulation and analysis of single negative metamaterial sensor based on microring resonator

Jun Sun (孙 俊)[1,2], Jinhui Peng (彭金辉)[1], Ming Huang (黄 铭)[2*],
Jiang Yu (余 江)[2], and Jingjing Yang (杨晶晶)[2]

[1]*Faculty of Metallurgical and Energy Engineering, Kunming University of Science and Technology, Kunming 650093, China*
[2]*Wireless Innovation Lab, School of Information Science and Engineering, Yunnan University, Kunming 650091, China*
Corresponding author: huangming@ynu.edu.cn

A novel microring resonator sensor coated with a single negative metamaterial (SNM) layer is proposed. The dispersion relation of hollow cylindrical dielectric waveguide covered with a SNM layer is derived, and resonant frequencies of the corresponding whispering gallery mode are computed. We find that there is a good agreement between the theoretical results and numerical results of resonant frequencies and electric field distributions. Compared with traditional resonator sensor, the sensitivity and resolution are significantly enhanced by SNM, and the Q factor can be tailored by adjusting the distance between the waveguide and the microring.

OCIS codes: 280.4788, 140.4780, 160.3918.
doi: 10.3788/COL201210.S22801.

Optical sensor based on whispering gallery mode (WGM) as an emerging sensing mechanism has recently attracted considerable attentions[1−4]. The sensing principle of this sensor is to detect a small change of the surrounding refractive index through the evanescent field traveling at its outer boundary, which is done by measuring the change of the resonance wavelength or optical intensity for fixed wavelength. It has been currently exploited in a wide variety of sensing applications[5−9] due to small size, high Q factor, and low detection limit. Examples of sensing applications of microring resonator include TNT detection from gas phase[10], biomedical and nano medicine field applications[11], HER2 extra-cellular domain breast cancer biomarker detection[12], and simultaneous measurement of refractive-index (RI) and temperature changes[13].

Metamaterial is a kind of material whose permittivity and/or permeability can be changed continuously from negative to positive values, and has received growing attention due to its extraordinary electromagnetic properties. It has widely applications, including cloak, perfect lens, concentrator, shrinking device and high perfor-

mance antenna, etc. Sensing application of metamaterials is another hot topic[14−18]. Recently, we found that metamaterials could significantly enhance the sensitivity and resolution of WGM resonator sensor[19−21]. In this letter, we propose another microring resonator sensor coated with a single negative metamaterial (SNM) layer. Theoretical analysis and full wave simulation of the SNM sensor have been demonstrated. Results show that the sensitivity of SNM sensor is much higher than that of the traditional microring resonator sensor, and the Q factor can be tailored for the sensitivity by regulating coupling distance.

Figure 1 shows the schematic diagram of a hollow cylindrical dielectric waveguide coated with a SNM layer. This waveguide is a four-region model. The relative permittivity and permeability of region 1, 2, 3, 4 are denoted as (e_1, m_1), (e_2, m_2), (e_3, m_3), and (e_4, m_4), respectively. The outside surface of the cylindrical dielectric waveguide (e_2, m_2) is covered with a SNM layer (e_3, m_3). The hollow core and the exterior region are free-space. Similar to Refs. [19–21], dispersion equation of the waveguide can be derived as

$$|M| = \begin{vmatrix} J_{\mathrm{m}}(p_1 r_1) & -J_{\mathrm{m}}(p_2 r_1) & -Y_{\mathrm{m}}(p_2 r_1) & 0 & 0 & 0 \\ -\dfrac{e_1 J'_{\mathrm{m}}(p_1 r_1)}{p_1} & \dfrac{e_2 J'_{\mathrm{m}}(p_2 r_1)}{p_2} & \dfrac{e_2 Y'_{\mathrm{m}}(p_2 r_1)}{p_2} & 0 & 0 & 0 \\ 0 & J_{\mathrm{m}}(p_2 r_2) & Y_{\mathrm{m}}(p_2 r_2) & -J_{\mathrm{m}}(p_3 r_2) & -Y_{\mathrm{m}}(p_3 r_2) & 0 \\ 0 & -\dfrac{e_2 J'_{\mathrm{m}}(p_2 r_2)}{p_2} & -\dfrac{e_2 Y'_{\mathrm{m}}(p_2 r_2)}{p_2} & \dfrac{e_3 J'_{\mathrm{m}}(p_3 r_2)}{p_3} & \dfrac{e_3 Y'_{\mathrm{m}}(p_3 r_2)}{p_3} & 0 \\ 0 & 0 & 0 & J_{\mathrm{m}}(p_3 r_3) & Y_{\mathrm{m}}(p_3 r_3) & -H_{\mathrm{m}}^{(1)}(p_4 r_3) \\ 0 & 0 & 0 & -\dfrac{e_3 J'_{\mathrm{m}}(p_3 r_3)}{p_3} & -\dfrac{e_3 Y'_{\mathrm{m}}(p_3 r_3)}{p_3} & \dfrac{e_4 H_{\mathrm{m}}^{'(1)}(p_4 r_3)}{p_4} \end{vmatrix} = 0, \quad (1)$$

where M can be derived from boundary continuity conditions of the four-region model. The functions J_{m},

Y_{m}, and $H_{\mathrm{m}}^{(1)}$ are, respectively, the Bessel functions of the first kind, the second kind, and the Hankel function
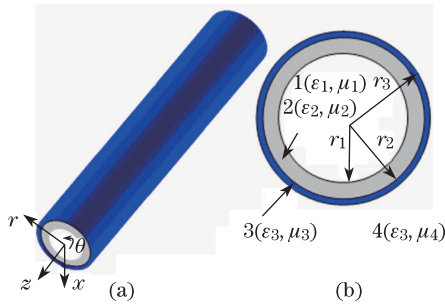
Fig. 1. (Color online) (a) Schematic diagram of a hollow cylindrical dielectric waveguide coated with a SNM layer (blue). r, θ, and z are the components of the circular cylindrical coordinates; (b) cross section of the waveguide with inner radius r_1, outer radius r_2, and thickness of SNM layer is $r_3 - r_2$.

of the first kind. The apostrophe signifies the derivative of the function with respect to its argument. The subscript m denotes the number of cyclic variations with the azimuthal coordinates. p_i can be expressed as $\omega\sqrt{e_i m_i}$, and ω is the angular frequency.

The simulation models of the microring resonator sensor are illustrated in Fig. 2. The sensing model A with air core ($e_1 = 1, m_1 = 1$) consists of a microring resonator, which is closely coupled with a straight waveguide of the same material ($e_2 = 10.24, m_2 = 1$) which serves as optical input and output for the device. The width of the ring and the waveguide is $w = 0.3$ μm. The microring resonator is 5 μm in outer diameter. The distance between the microring and the waveguide is $g = 0.35$ μm. The sensing models A and B serve for homogeneous sensing and surface sensing. The SNM sensing model C and D serve for homogeneous sensing and surface sensing. The permittivity and permeability of the SNM layer are $e_3 = 1, m_3 = -1$. In the following sections, we simulate the performance of these sensors using a commercial software COMSOL multiphsics. In the simulations, the computational space is surrounded by scattering boundary. The excitation is set at port A of the waveguide. The spectrum is obtained by frequency sweep. The computational domain is meshed using a triangle grid. The mesh size, the maximum element size, used in this model is 0.02 μm in the waveguide and microring, 0.04 μm in air, and 0.01 μm in the SNM layer.

By frequency sweep in the range of $185-212$ and $175-200$ THz, the spectra of the microring resonator without and with a SNM layer ($t_m = 0.09$ μm) are shown in Fig. 3. The spectral lines from left to right represent first-order radial WGM with $m = 25, 26, 27, 28$, and 29, respectively. It can be seen that the spectral lines are broadened when the resonator is coated with a SNM layer, and the maximum normalized. electric field intensity of Model A is about 6.67 times larger than that of Model C. The insets of Figs. 3(a) and (b) are the zoomed versions of the spectral lines of mode 27 for better observation.

The analytical and numerical electric field distributions of the microring resonator without and with a SNM layer are presented in Fig. 4. The azimuthal mode number $m = 27$ is the period of field change along the periphery of the microring resonator, and its mode is formed by the circulation of electromagnetic wave within the microring. It can be observed that the numerical

field distribution is in good agreement with analytical field distribution, and stronger evanescent field penetrating into the periphery of the microring resonator will make the sensing model C more sensitive to detect any external perturbation. This indicates that the evanescent field of the detection area is enhanced by the SNM layer.

The analytical and numerical resonant frequencies and the Q factors of each mode of the microring resonator in Fig. 3 are summarized in Table 1. It can be
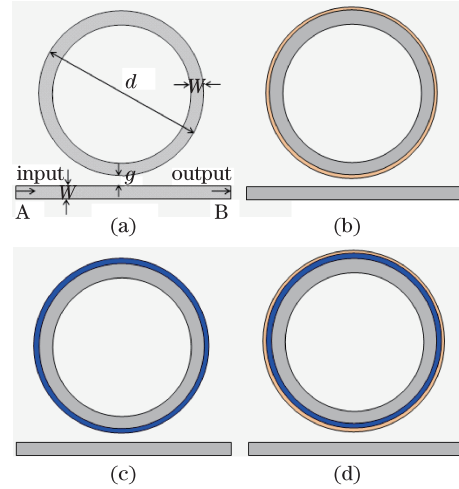

Fig. 2. Simulation models of the microring resonator sensor. (a) Microring resonator sensor (colored in grey) for homogeneous sensing (Model A); (b) microring resonator sensor for surface sensing (Model B), analytes are colored in tan, and its thickness is t_f; (c) SNM sensor for homogeneous sensing (Model C), SNM layer is colored in blue, and its thickness is t_m; (d) SNM sensor for surface sensing (model D).
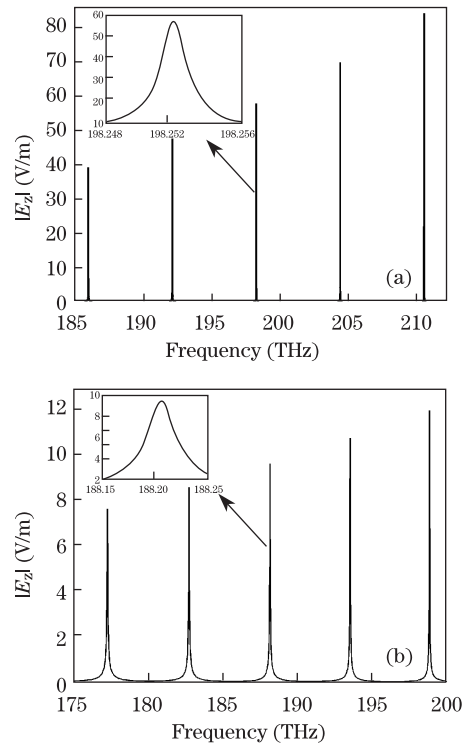

Fig. 3. Resonant frequency spectra of the sensing model A (a) and model C (b).

Table 1. Analytical Resonant Rrequency (f_{0a}), the Numerical Resonant Frequency (f_{0n}) and Q Factor of Model A and Model C

Mode (m)		25	26	27	28	29
Model A ($t_m = 0$ μm)	f_{0a} (THz)	186.12	192.2	198.25	204.3	210.35
	f_{0n} (THz)	186.15	192.2	198.25	204.3	210.35
	Q	76 092.69	113 391.76	168 559.06	249 137.52	366 534.41
Model C ($t_m = 0.09$ μm)	f_{0a} (THz)	177.32	182.78	188.2	193.57	198.88
	f_{0n} (THz)	177.33	182.79	188.21	193.57	198.88
	Q	4 779.48	6 245.88	8 109.6	10 265.63	13 653.25
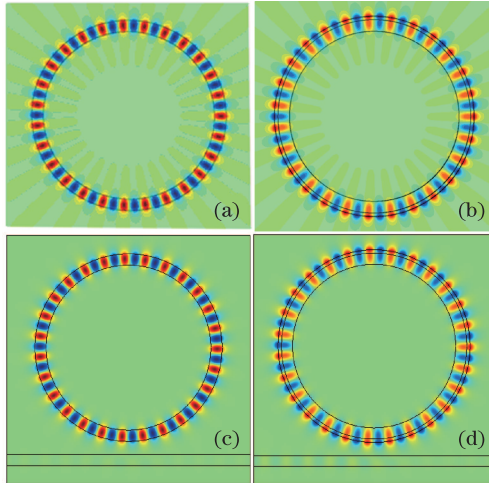
Fig. 4. (Color online) Visualizations of the steady-state electric field distribution in the microring resonator sensor ($m = 27$) of model A and model C. (a) and (b) Analytical results, (c) and (d) numerical results.

seen that the Q factor of the sensing model C is much lower than that of the model A, which indicates that the Q factor of the model A after adding a SNM layer decreases. Meanwhile, the analytical resonant frequencies of the sensing model A and C agree well with numerical results. These results confirm the effectiveness of the method we have developed.

To further confirm evanescent field amplification phenomenon, we have investigated the spectra of mode 27 for homogeneous and surface sensing with respect to the different ambient medium permittivities ε_r (from 1 to 1.1 with small intervals of 0.02), as shown in Figs. 5 and 6, respectively. It shows that the resonance frequency decreases with an increase of the ambient medium permittivity. The change of permittivity of analytes adsorbed on the surface of the sensor interacting with WGMs results in a change of effective refractive index and radius of the WGM modes, and in turn leads to a shift in the WGM spectral position. In the case of homogeneous sensing, which is to detect the analytes homogeneously surrounding the sensor, the sensitivities for sensing model A and model C are 13.8 and 111.1 nm/RIU, respectively. Here, sensitivity is defined as $d\lambda/dn = [\lambda(e_r, t_m) - \lambda(1, t_m)]/(\sqrt{e_r} - 1)$. Obviously, the sensitivity of sensing model C is about 8.05 times larger than that of model A. In the case of surface sensing, which is to detect the analytes specifically adsorbed on the surface of the sensor, the sensitivities of sensing

model B and model D are 8.3 and 66.2 nm/RIU, respectively. Thus the sensitivity of sensing model D is about 8 times larger than that of model B. Therefore, the SNM sensor has significantly enhanced sensitivity.

To further investigate the performance of the sensor, the resonant wavelength shift has been simulated as a function of the ambient medium permittivity ε_r for different thicknesses of SNM and analytes, as shown in Figs. 7 and 8. Resonant wavelength shift is calculated by $d\lambda = \lambda(e_r, t_{m,f}) - \lambda(1, t_{m,f})$. From Fig. 7, the wavelength shift increases monotonically with e_r, and the thicker the metamaterial layer is, the larger the wavelength shift is in both homogeneous sensing and surface sensing. Take the SNM sensor ($t_m = 0.15$ μm) and microring resonator sensor for example: in term of homogeneous sensing, the sensitivity of the SNM sensor (Model C) for ε_r from 1 to 1.1 (colored in pink) is about 285.5 nm/RIU, and for the microring resonator sensor (Model A) is about 13.8 nm/RIU (colored in blue), so the sensitivity of the SNM sensor is about 20.7 times larger
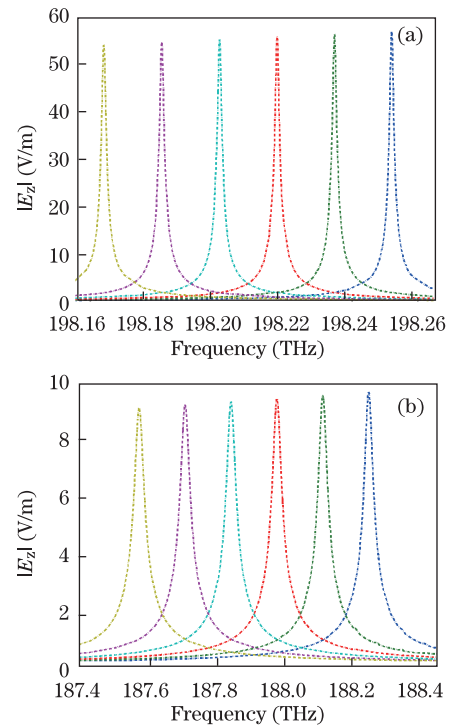

Fig. 5. Resonant frequency spectra of mode 27 with respect to different ambient medium permittivities ε_r for homogeneous sensing. From right to left, the spectra correspond to ε_r from 1 to 1.1 with intervals of 0.02, respectively. (a) Sensing Model A; (b) Model C ($t_m = 0.09$ μm).
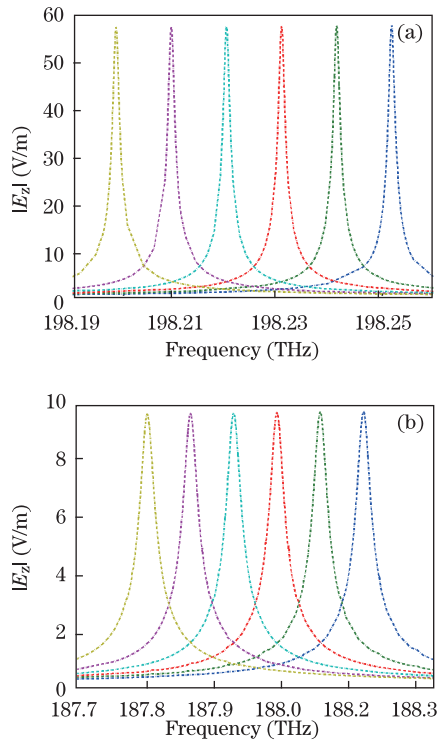
Fig. 6. Resonant frequency spectra of mode 27 with respect to different ambient medium permittivities ε_r for surface sensing. From right to left, the spectra correspond to ε_r from 1 to 1.1 with intervals of 0.02, respectively. (a) Sensing Model B ($t_f = 0.05$ μm); (b) model D ($t_f = 0.05$ μm, $t_m = 0.09$ μm).
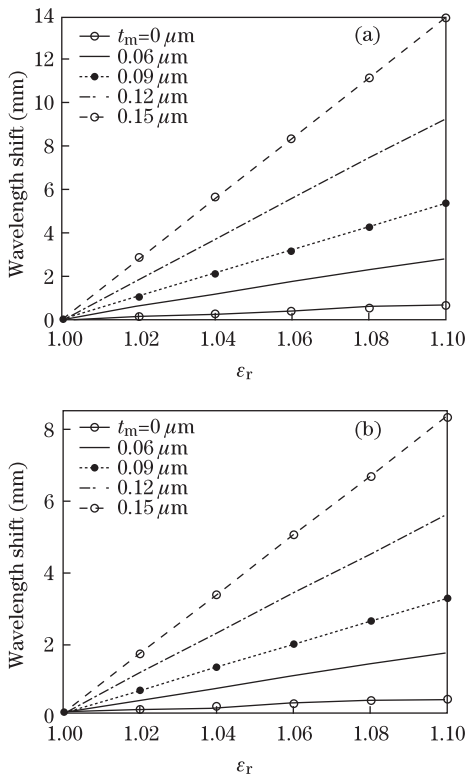
than that of the microring resonator sensor; in term of surface sensing, the sensitivity of the sensing model D ($t_f = 0.05$ μm) for ε_r from 1 to 1.1 (colored in pink) is about 170.1 nm/RIU, and for the model B ($t_f = 0.05$ μm) is about 8.3 nm/RIU (colored in blue), then the sensitivity of the SNM sensor (Model D) is about 20.5 times larger than that of model B.

Figure 8 shows those simulation results of the surface sensing for different thicknesses of analytes. It is seen that the thicker the analytes is, the larger the wavelength shift is. The wavelength shift and the sensitivity of the SNM sensor are about 8 times larger than that of microring resonator sensor.

From the above the results, we find that the sensitivity of the SNM sensor is enhanced, but the Q factor is decreased. To find a method to increase the Q factor, we study the effects of the coupling gap on the Q factor. Figure 9 shows the relationship between the coupling gap and the maximum normalized electric field intensity $|E_z|_{max}$ and Q factor. It is observed that there are two peaks b and e. $|E_z|_{max}$ of point b is about 9.153 V/m while for point e it is about 9.741 V/m, and both have higher Q factor. The trend of curve $Q - g$ is in line with $|E_z|_{max} - g$ before point e, but after point e the Q factor directly tends to be constant. It shows that the corresponding gap in the vicinity of point e is a good coupling distance, which has higher Q factor and the maximum normalized electric field.

To further explain this phenomenon, we portray the electric field distributions of peaks a–f shown in Figs. 10(a) to (f) respectively. For points a and c, the maximum normalized electric field and Q factor are small,
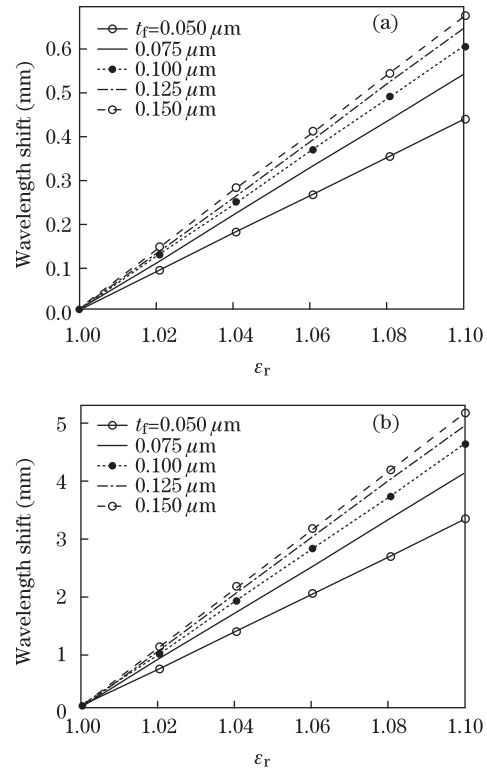

Fig. 7. Wavelength shifts against the ambient medium permittivities ε_r with respect to the different SNM thicknesses t_m. (a) Homogeneous sensing; (b) surface sensing ($t_f = 0.05$ μm).

Fig. 8. Wavelength shift against the ambient medium permittivities ε_r with respect to the different analytes thicknesses t_f for surface sensing. (a) Microring resonator sensor; (b) SNM sensor ($t_m = 0.9$ μm).

and this is over-coupling. For point b, the maximum normalized electric field and Q factor are high, but they are very sensitive to the coupling gap, and difficult to implement. For point f, the Q factor is high, but the electric field is very weak, and this is under-coupling. This indicates that WGM cannot be excited in the microring shown in Fig. 10(f). Therefore, these coupling gaps are not suitable for the SNM sensor. For near point e, the electric field around the microring is strong as shown in Figs. 10(d) and (e), and the Q factor of the SNM sensor is high, thus, it is a suitable coupling gap. These conclusions are confirmed by S parameter shown in Fig. 11. It indicates that when the coupling gap is about 0.38 μm, S_{21} has a minimum value, where higher power of electromagnetic wave is coupled into the microring. Figure 12 shows the deviations of numerical resonant frequency to the analytical frequencies f_a (eigenfrequency) with different g, where the deviation is defined as $d = |f_n - f_a|/f_a$.
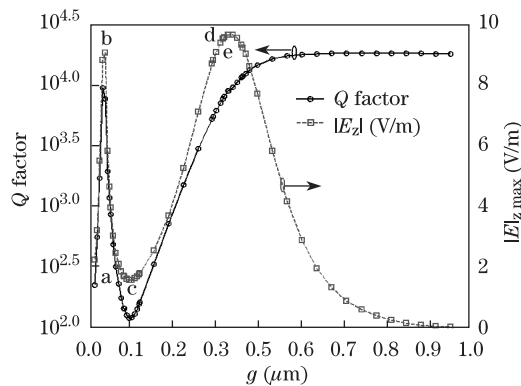

Fig. 9. Effects of the coupling gap g on the Q factor and the maximum normalized electric filed $|E_z|_{max}$.
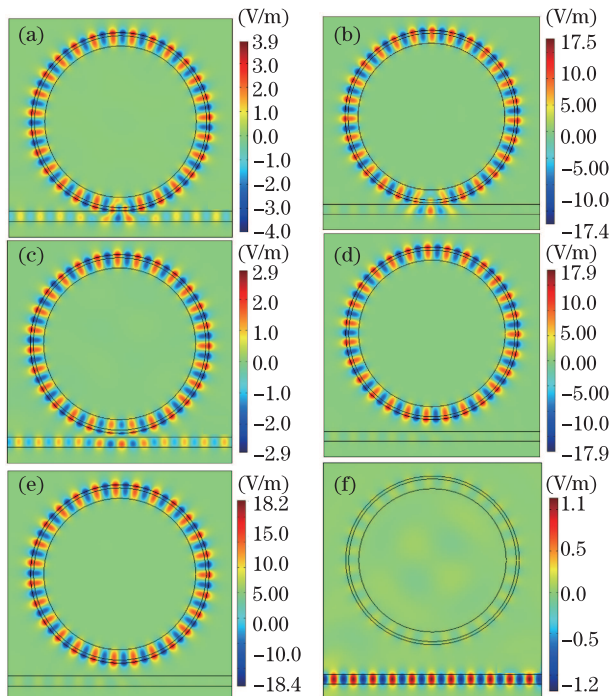

Fig. 10. Steady-state electric field distributions of SNM sensor ($m = 27$) for different values of coupling gap. (a) $g = 0.01$ μm, (b) $g = 0.0382$ μm, (c) $g = 0.1018$ μm, (d) $g = 0.35$ μm, (e) $g = 0.3625$ μm, and (f) $g = 0.7150$ μm.
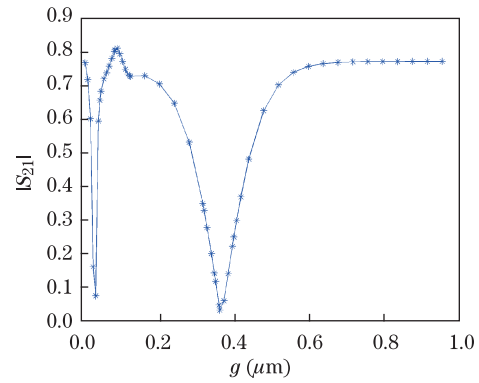

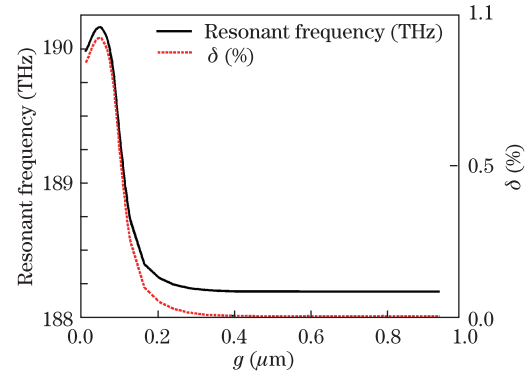Fig. 11. Effects of the coupling gap on S_{21}.

Fig. 12. Resonant frequencies and their deviations to the analytical frequency f_a (eigenfrequency) with different g.

When the coupling gap increases, the numerical resonant frequency will tend to be a stable eigenfrequency 188.2 THz.

In conclusion, WGMs of the dielectric waveguide with a SNM layer are theoretically analyzed, and the dispersion relation is derived. Analytical results of the resonant frequency and electric field distribution of the sensor are in good agreement with the numerical results. We show that the sensitivities of the SNM sensor for homogeneous sensing and surface sensing are about 8 times larger than those of microring resonator sensor, and Q factor can be tailored. Moreover, the sensitivity is further improved by increasing the thickness of the SNM layer. It opens an avenue for designing novel sensors with desired sensitivity using SNM.

References

1. D. K. Armani, T. J. Kippenberg, S. M. Spillane, and K. J. Vahala, Nature **421,** 925 (2003).
2. K. J. Vahala, Nature **424,** 839 (2003).
3. A. M. Armani, R. P. Kulkarni, S. E. Fraser, R. C. Flagan, and K. J. Vahala, Science **317,** 783 (2007).
4. F. Vollmer and S. Arnold, Nat. Methods **5,** 591 (2008).
5. N. Mohammad, C. Huanyu, G. Suren, S. Daryoosh, and S.-N. Safieddin, Meas. Sci. Technol. **21,** 015202 (2010).

6. E. Tcherniavskaia and V. Saetchnikov, J. Appl. Spectrosc. **77,** 692 (2010).

7. Q. L. Ma, T. Rossmann, and Z. X. Guo, Meas. Sci. Technol. **21,** 025310 (2010).

8. N. Lin, L. Jiang, S. M. Wang, H. Xiao, Y. F. Lu, and H. L. Tsai, Appl. Opt. **50,** 992 (2011).

9. J. Knittel, T. G. McRae, K. H. Lee, and W. P. Bowen, Appl. Phys. Lett. **97,** 123704 (2010).

10. R. Orghici, P. Lüzow, J. Burgmeier, J. Koch, H. Heidrich, W. Schade, N. Welschoff, and S. Waldvogel, Sensors **10,** 6788 (2010).

11. A. Haddadpour and Y. Yi, Biomed. Opt. Express **1,** 378 (2010).

12. J. T. Gohring, P. S. Dale, and X. Fan, Sensor. Actuat. B-Chem. **146,** 226 (2010).

13. N. Lin, L. Jiang, S. M. Wang, L. Yuan, and Q. H. Chen, Chin. Opt. Lett. **10,** 052802 (2012).

14. A. V. Kabashin, P. Evans, S. Pastkovsky, W. Hendren, G. A. Wurtz, R. Atkinson, R. Pollard, V. A. Podolskiy, and A. V. Zayats, Nat. Mater. **8,** 867 (2009).

15. H. Tao, A. C. Strikwerda, M. Liu, J. P. Mondia, E. Ekmekci, K. Fan, D. L. Kaplan, W. J. Padilla, X. Zhang, R. D. Averitt, and F. G. Omenetto, Appl. Phys. Lett. **97,** 261909 (2010).

16. Z. G. Dong, H. Liu, J. X. Cao, T. Li, S. M. Wang, S. N. Zhu, and X. Zhang, Appl. Phys. Lett. **97,** 114101 (2010).

17. Y. Li, X. Tao, H. Chen, and W. Y. Tam, J. Opt. Soc. Am. A **28,** 314 (2011).

18. M. Huang and J. J. Yang, *Wave Propagation*, A. Petrin, (eds.) (InTech Inc., Austria, 2011) pp. 13.

19. M. Huang, J. J. Yang, S. Jun, S. J. Mu, and Y. Z. Lan, Sensors **11,** 5886 (2011).

20. J. Sun, M. Huang, J. J. Yang, T. H. Li, and Y. Z. Lan, Sensors **11,** 8060 (2011).

21. J. J. Yang, M. Huang, and J. Sun, IEEE Sensor J. **11,** 2254 (2011).